Broadband interferometric subtraction of optical fields

T. BUBERL,[1] P. SULZER,[2] A. LEITENSTORFER,[2] F. KRAUSZ,[1,3] AND I. PUPEZA[1,3,*]

[1]*Max Planck Institute of Quantum Optics, Hans-Kopfermann-Straße, 1 85748, Garching, Germany*
[2]*Department of Physics and Center for Applied Photonics, University of Konstanz, 78457, Konstanz, Germany*
[3]*Ludwig-Maximilians-Universität München, Am Coulombwall 1, 85748, Garching, Germany*
[*]*ioachim.pupeza@mpq.mpg.de*

Abstract: We present a Mach-Zehnder-like interferometer capable of simultaneous super-octave (950 – 2100 nm) destructive interference with an intensity extinction of 4×10^{-4}. Achromatic nulling is achieved by unbalancing the number of Fresnel reflections off optically denser media in the two interferometer arms. With a methane gas sample in one interferometer arm, we isolate the coherent molecular vibrational emission from the broadband, impulsive excitation and quantitatively examine the potential improvement in detectable concentration, compared to direct transmission geometry. The novel concept will benefit sensing applications requiring high detection sensitivity and dynamic range, including time-domain and frequency-domain spectroscopy.

1. Introduction

In traditional spectroscopic techniques, the signal associated with the process under scrutiny manifests as a change of the radiation source intensity (or field). This imposes two main limitations on the smallest detectable signal: Firstly, its magnitude is lower-bound by excess source noise. Secondly, resolving a small change of a comparatively large signal requires high-dynamic-range detection.

In the field of Fourier transform infrared (FTIR) spectroscopy, the idea of a dual-beam approach to overcome part of these limitations was first realized by Bar-Lev [1] in 1966. He utilized both the interferogram and the anti-interferogram beam produced by an FTIR spectrometer and measured the resulting difference signal with a balanced detector. Later works inserted a reference and a sample into each beam and focused both outputs on a single detector [2,3], which results in the cancellation of the common AC-components of the opposing interferograms. In doing so, the effect of excess source noise on the detection limit can be in principle suppressed down to the shot-noise level of the source [4]. Because sequential measurements of sample and reference signal become unnecessary, the measurement time and systematic errors are reduced and the dynamic range requirements of the digitization electronics are relaxed [5]. However, none of the various dual-beam FTIR schemes [1–6], addressed the issue of the limited dynamic range of the detector because the DC-component of the interferograms was always present. In contrast, *optically* subtracting a reference signal *before* detection spatially isolates the sought-for signal, disclosing it in front of a quasi-zero background. This can be realized by an interferometer in whose arms the propagation of light differs precisely by the process under scrutiny [7]. Ideally, in the interferometer port combining both arms with opposing phase, only the (miniscule) differences do not interfere destructively [8]. Thereby, the cancellation of the – usually orders of magnitude stronger – reference signal facilitates excitation intensities far above the saturation limit of the detector. Thus, the amplitude of the detected sample response can always be raised above the detector and shot noise levels. In particular, interferometric,

optical subtraction facilitates the direct comparison of two samples by increasing the visibility of slight differences between their spectra.

To adapt interferometric, optical subtraction for broadband frequency-domain and ultrafast, time-domain spectroscopy (which by definition is broadband) the challenge of simultaneous cancellation of super-octave spectra has to be addressed. In this paper, we present a Mach-Zehnder-type interferometer, with an unprecedented combination of broad bandwidth (950 nm - 2100 nm) and achromatic intensity suppression (4×10^{-4}). Compared to the more complex approaches developed, e.g., for the direct observation of extrasolar planets [9], our concept for achromatic nulling solely relies on the combination of Fresnel reflections off boundaries between media with different refractive indices. In a proof-of-principle experiment of differential molecular fingerprinting, we spatially isolate the resonant response of a molecular sample to an impulsive, linear excitation from the instantaneous sample response, carrying negligible fingerprint information.

A phase shift between two interferometer arms can be achieved by increasing the length of one arm with respect to the other. The acquired phase shift $\Delta\varphi$ is given by:

$$\Delta\varphi = 2\pi \frac{\Delta l}{\lambda}, \tag{1}$$

where Δl is the difference in optical path length and λ the wavelength. For broadband destructive interference, a wavelength-independent phase shift of π between the interfering electro-magnetic fields is necessary. As Eq. (1) shows, the phase shift due to mutual delaying however, is always wavelength dependent.

Several solutions for achromatic phase shifting have been developed in the field of observational astronomy [10]. For instance, a pair of mirror-symmetric periscopes can be used to geometrically implement a phase shift [11], the Gouy phase shift introduced by an additional focus in one arm can be exploited [12], and a pair of right-angle Fresnel rhombs acts as achromatic quarter-wave plates [13]. However, all these concepts are either technically complex or not suitable for ultrashort-pulse applications. Here, we adapt a simple concept, employed by Hayden et al. [14] for spectral absorption and dispersion measurements of a liquid sample with a tunable narrowband laser, to broadband, achromatic nulling.

2. Interferometric setup

The experimental setup is sketched in Fig. 1. Apart from two adaptations, our setup is equivalent to a Mach-Zehnder interferometer with uncoated surfaces for beam splitting and combining. In the latter, an achromatic phase difference of π between the interferometer arms is caused by the fundamental property of light waves undergoing no phase change when reflected off a boundary to a medium with lower refractive index. However, light propagating to the destructive port of such an interferometer is reflected three times in one arm and transmitted twice and reflected once in the other arm, which leads to imperfect cancellation for broadband radiation due to refractive index changes. Therefore, here we combine an equal number of reflections and transmissions in each arm in the destructive port. For achromaticity, the resulting additional material passage in arm 1 is exactly compensated for by adding a window twice as thick as the beam combiner in arm 2. In the upper output port of the interferometer in Fig. 1, the interfering light has opposing phase because the light is reflected off the first surface of the beam splitter in arm 1 and off the second surface of the beam combiner in arm 2.

The interferometer employs plane, 3-mm thick borosilicate crown glass (N-BK7) windows for beam splitting and combining. The substrate thickness and material were chosen to provide reasonable spatial separation between the reflection off the first and the second surface for spatially filtering of undesired multiple reflections. The angle of incidence on the windows is 60°, providing a reflectivity of approximately 18% for s-polarized light which is close to the optimum splitting ratio of 20:80 for maximized power in the destructive port (see

Appendix). For symmetry reasons, small pointing fluctuations of the incident beam do not affect the extinction. For stabilization of the optical path difference (OPD), the length of arm 1 is controlled via a feed-back loop acting on a piezo-electric transducer (PZT). A Hänsch-Couillaud error signal [15] is generated using an auxiliary laser which exactly follows the beam path of the main laser, except for an offset in beam height. The input polarization of the auxiliary laser is linear with 45° rotation with respect to the propagation plane, so that both arms acquire a polarization change in the constructive port (two transmissions in arm 2 and two reflections in arm 1).

Our experiments were carried out with a super-octave spectrum generated by a femtosecond Er:fiber laser system. The commercial oscillator-amplifier combination operates at a repetition rate of 56 MHz. The 90-fs output is coupled into a highly nonlinear fiber assembly, and spectrally broadened. Temporal compression results in a pulse duration of 11 fs spanning a spectrum between 950 nm and 2100 nm with 175 mW of average power (for details see [16]).

It is noteworthy that our interferometer design is not specific to ultrashort, pulsed laser sources and can in general be adapted to any kind of light source (including, e.g., thermal sources) if the transmissive optics are selected according to the desired wavelength range.
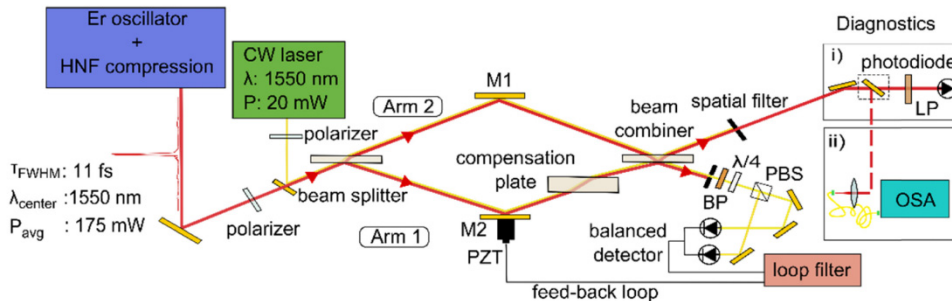

Fig. 1. Mach-Zehnder-type interferometer: Light entering the interferometer is partially reflected and partially transmitted at the first surface of the beam splitter. The reflected part passes through the compensation plate and is partially reflected off the first surface of the beam combiner. The transmitted part is partially reflected off the second surface of the beam combiner. The destructive port of the interferometer is sent to the diagnostics, whereas the constructive port is used to generate a Hänsch-Couillaud error signal from an auxiliary laser. Through the interferometer we propagated 11-fs input pulses spanning from 950 nm to 2100 nm, generated from an erbium fiber laser system. BP: Band pass filter, FWHM = 12 nm at 1550 nm. PBS: Polarizing beam splitter. LP: 950 nm longpass filter. OSA: Optical spectrum analyzer.

3. Theoretical limitations of interferometric extinction

Besides equal arm length, the alignment of the optical components within the interferometer is critical for achromatic nulling. Ideally, all optical surfaces should be parallel to each other and substrate thicknesses should match to minimize the influence of transverse misalignment, and unbalance of intensity and dispersion. Figure 2(a) shows the calculated influence of angular misalignment on the spatial overlap of both 30-cm-long arms after recombination, which identically translates into a degradation of the extinction ratio (see Appendix). According to our calculations, a misalignment of any optical element has the same quantitative influence on the extinction ratio. For longer arm length, the alignment sensitivity increases. With the precision of commercially available motorized kinematic mounts (1 μrad) an extinction ratio of 6×10^{-6} for a central wavelength of 1550 nm and 6×10^{-7} for 10-μm central wavelength is in principle attainable if only the spatial overlap is considered.

In addition to the alignment, the extinction ratio is influenced by dispersive effects owing to substrate thickness variations. Figure 2(b) shows that the influence of substrate thickness mismatch decreases for increasing pulse duration. The shaded orange area corresponds to

thickness tolerances typically specified by manufacturers. If the worst combination of thickness mismatch (0.9 mm between arm 1 and 2) is considered, the extinction ratio for 10-fs input pulses is limited to 2×10^{-4}.
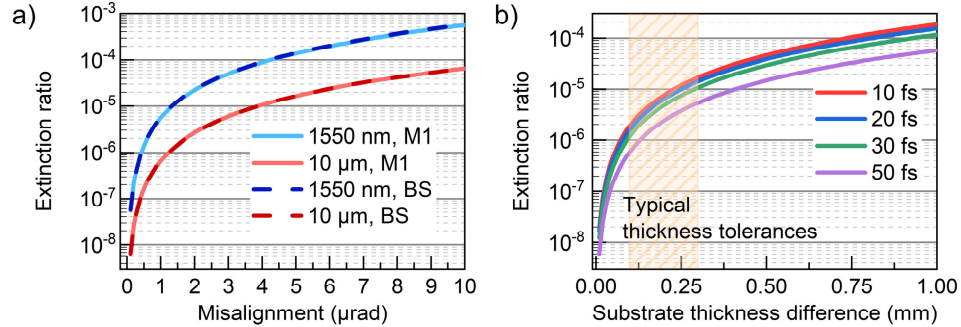

Fig. 2. (a) Simulated decrease of extinction ratio for misalignment of two different optical elements in the interferometer at 1550 nm and 10 µm central wavelength. (b) Simulated decrease of extinction ratio depending on the difference in substrate thickness of beam splitter and beam combiner for different input pulse durations. Shaded area: typical thickness tolerances specified by the manufacturer.

4. Experimental interferometric extinction

In the experiment, the performance of the interferometer was characterized by recording the signal at the destructive port with a photodiode (PD) while applying a saw-tooth voltage to the PZT to scan the OPD through zero. Far from OPD = 0 a calibrated neutral density filter was applied to ensure a linear response of the PD. Ideally, the interfering fields E_1 and E_2 are identical and the following equality holds:

$$I_{con} = \left| E_1 + E_2 \right|^2 = \left| 2E_1 \right|^2 = 4I_1 \tag{2}$$

where I_{con} is the intensity of the ideal constructive interference and I_1 is the intensity of one arm. We measured the voltage corresponding to the intensity of one arm and divided the recorded signal during destructive interference by four times this value. The resulting extinction ratio reaches a minimum of 4.2×10^{-4}. This value is in good agreement with the computed values given the limited precision of manual alignment and the presence of air fluctuations in our experiment.

It is worth noting that broadband constructive interference cannot be reached in the port designed for destructive interference, because a modification of the OPD will result in a wavelength-dependent phase difference between the two interferometer arms.

Figure 3(a) shows a comparison of the locked and the free-running PD signal at the destructive port of the interferometer on a timescale of 30 s. In the locked state, the root mean square (RMS) value of the extinction ratio is 6.1×10^{-4}. Comparing the standard deviation of the free-running and the locked PD signal reveals a reduction of the fluctuations of the extinction ratio by almost one order of magnitude from 6.4×10^{-4} in the free-running to 7.2×10^{-5} in the locked state. The discrepancy between the values of the extinction ratio in the scanned and in the locked state is most likely caused by differing air fluctuations in the two arms of the interferometer, which cannot be removed by the 1-dimensional PZT lock.

To investigate the wavelength dependence of the extinction, the stabilized signal was sent to an optical spectrum analyzer (OSA). The power spectral densities (PSD) of the destructive and the ideal constructive interference (defined as four times the PSD from a single arm) are depicted in Fig. 3(b). The RMS value of the spectrally resolved extinction ratio of 6.2×10^{-4} is in excellent agreement with that of the spectrally integrated extinction ratio determined with the PD.
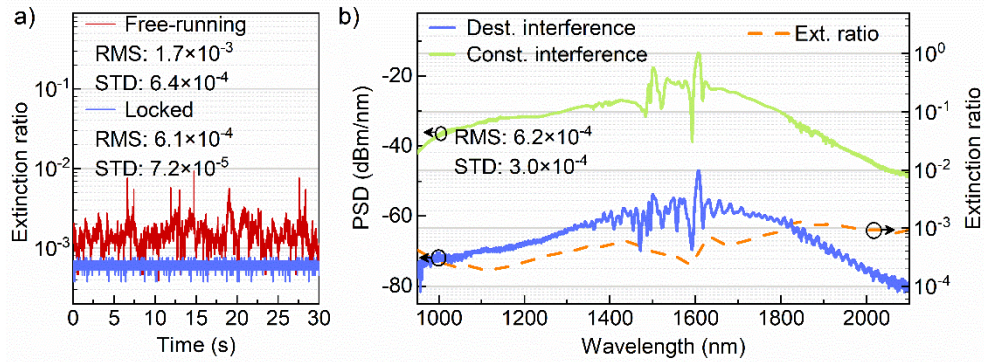
Fig. 3. (a) Extinction ratio measured with a photo diode for the free-running interferometer and the interferometer locked via the Hänsch-Couillaud error signal. (b) Spectrally resolved constructive and destructive interference. The modulation of the destructive interference spectrum at constant frequency corresponds to the thickness of the beam splitter/ combiner and can be explained by imperfect spatial filtering of multiple reflections in the substrate(s). The dashed orange curve shows the extinction ratio calculated by integrating the PSD in steps of 40 nm and dividing the destructive by the constructive PSD. The integration avoids extrema due to non-coinciding modulations in the two signals arising from the fact that the destructive interference lies only slightly above the detector noise of the OSA and therefore shows stronger fluctuations than the constructive interference.

5. Sensitivity improvement for differential spectroscopy

In the following, we discuss the potential afforded by this interferometric extinction for spectroscopic applications. To quantitatively investigate the advantages of the differential measurement over the direct one, regarding dynamic range and detection sensitivity, in the following we derive expressions for the signal strength (i.e. power in a given spectral element) associated purely with the light-matter interaction and for the noise background, for the direct and the differential measurement case, in analogy to [14]. In the direct measurement, for each spectral element the power attenuation in a molecular sample is given by Beer's law:

$$P_{(S,dir)} = P_0 e^{-A} \qquad (3)$$

where P_0 is the power recorded by the detector without sample, $P_{S,dir}$ is the power recorded with sample, and A is the attenuation which is linearly proportional to the sample thickness, the absorption cross section, and the concentration. For simplicity, we do not include the complex molecular response here assuming that the considered concentrations are so small that the influence of phase effects is negligible with respect to the extinction ratio. Note, that in our experiment the "reference power" P_0 is that of the laser beam, after propagation along the empty sample arm when the other arm is blocked, and constitutes the background in the direct measurement. Furthermore, the two power values refer to the nominal levels, i.e. do not account for noise. Then, the difference between P_0 and $P_{S,dir}$ yields a signal which can be associated purely with the light-matter interaction in the sample arm, which we henceforth refer to as "molecular signal" $P_{M,dir}$:

$$P_{(M,dir)} = P_0 - P_{S,dir} = P_0(1 - e^{-A}). \qquad (4)$$

This signal vanishes in the limit $A \to 0$. Furthermore, in the above equation the background P_0 can be interpreted as $P_0 = \lim_{A \to 0}(P_{S,dir})$, which holds in a more general sense. The amplitudes E of the electric fields involved are connected to the measured powers P via the equality

$E = c\sqrt{P}$, with some proportionality constant c. Thus, for the electric field amplitude $E_{S,dir}$ the following equation can be derived:

$$E_{(S,dir)} = c\sqrt{P_{S,dir}} = E_0 e^{-A/2},$$ (5)

where $E_0 = c\sqrt{P_0}$. To model the differential measurement, we consider the overlap of the electric fields E_1 and E_2 in the two interferometer arms, with opposing phase and a small difference δ in field amplitude describing the imperfect extinction. According to the definition of the extinction ratio Δ, the unbalance factor δ is given by $\delta = \sqrt{4\Delta}$. In the following, we account for the unbalance by reducing the amplitude of E_1 with respect to the ideal case. Thus, after transmission through the sample, the field amplitude E_1 reads:

$$E_1 = E_0(1-\delta)e^{-A/2}$$ (6)

and the reference field amplitude E_2 is E_0. The electric field amplitude at the destructive port of the interferometer $E_{S,diff}$ is given by:

$$E_{S,diff} = E_2 - E_1$$ (7)

and the power $P_{S,diff}$ arriving at the detector is:

$$P_{S,diff} = \frac{1}{c^2} E^2_{S,diff} = P_0\left(1-(1-\delta)e^{-A/2}\right)^2.$$ (8)

In analogy to the argumentation for the direct signal, the molecular signal in the differential measurement is given by:

$$P_{M,diff} = P_{S,diff} - \lim_{A \to 0}(P_{S,diff})$$
$$= P_0\left(\left(1-(1-\delta)e^{-A/2}\right)^2 - \delta^2\right).$$ (9)

For both cases – direct and differential measurement – to determine the weakest detectable attenuation A, the molecular signals, as derived in Eq. (4) and Eq. (9), need to be, compared to the respective noise powers. For modeling the latter, we consider intensity noise of the laser source P_L, shot noise P_{SN}, and detector noise P_{det} as uncorrelated contributions to the total noise power P_N [8]:

$$P_N = \sqrt{P_L^2 + P_{SN}^2 + P_{det}^2}.$$ (10)

The total noise power $P_{N,dir}$ in the direct measurement is given by:

$$P_{N,dir} = \sqrt{\left(\sigma P_{S,dir}\right)^2 + \frac{P_{S,dir}\,h\nu}{T} + \left(P_{det}\right)^2},$$ (11)

where σ is the relative intensity noise of the source (in our experiment 0.21%, determined as the relative standard deviation of 70 measurements of P_0 with the OSA at 1645 nm), h is Planck's constant, ν is the optical frequency, and T is the measurement time for the respective spectral element. Accordingly, the total noise power $P_{N,diff}$ is given by:

$$P_{N,diff} = \sqrt{\left(\sigma P_{S,diff}\right)^2 + \frac{P_{s,diff}\,h\nu}{T} + \left(P_{det}\right)^2}.$$ (12)

Here, we assume an ideal lock, i.e. that the mean extinction ratio Δ is maintained over the entire measurement time. Note that the shot noise in our classical, linear optical system is proportional to the square root of the number of photons arriving at the detector.

To be detectable, the molecular signal has to be larger than the total noise power, which leads to the following inequalities:

$$P_{M,dir} > P_{N,dir} \tag{13}$$

and

$$P_{M,diff} > P_{N,diff}. \tag{14}$$

Setting the lhs equal to the rhs in Eq. (13) and Eq. (14) and solving for the attenuation A reveals the smallest detectable attenuation in the direct and differential case depending on the input power, the extinction ratio, and the relative intensity noise. Note that in this derivation we accounted for the interferometer unbalancing by reducing the electric field E_1 in the sample arm by the factor $(1-\delta)$, see Eq. (6). A similar derivation can be performed by reducing E_2. While this leads to a slightly different strength of the molecular signal, this difference is negligible for most practical cases.

Figure 4(a) shows the calculated limit of detection (LOD) defined as the minimum detectable attenuation for increasing power per spectral element in the direct and differential configuration for an extinction ratio of 6×10^{-4}, considering a 10^{-3}-nm broad spectral element centered at 1545 nm and a measurement time of 10 ms for this spectral element. The magnitude of the different noise contributions to the LOD is also shown in Fig. 4(a). In general, the influence of detector noise and shot noise on the LOD decreases with increasing power, i.e., number of photons, but the influence of intensity noise is constant. Thus, for all configurations, the reachable LOD is ultimately limited by the intensity noise. However, detector saturation sets a significantly stronger constraint on increasing the power in the direct configuration, whereas in differential measurements the power reaching the detector predominantly consists of signal specific to the light-matter interaction under scrutiny. In the latter case, the incident power can exceed the saturation limit of the detector by orders of magnitude.
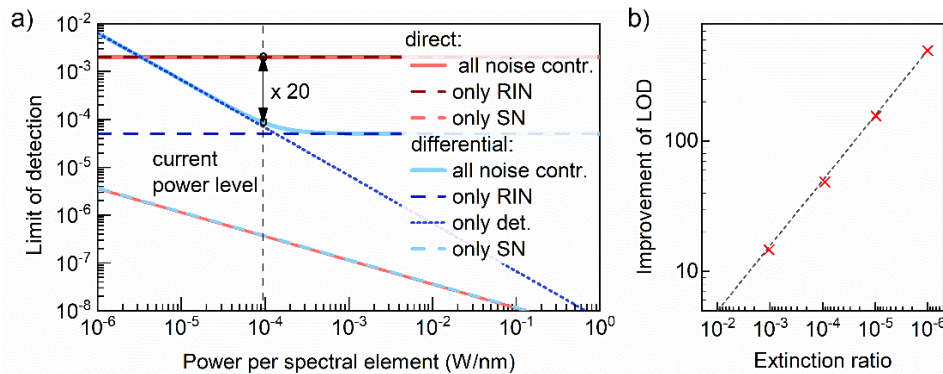

Fig. 4. (a) Calculated limit of detection for increasing power per spectral element in the direct and the differential configuration for an extinction ratio of 6×10^{-4} and a constant relative intensity noise (RIN) of 0.2%. SN: shot noise. (b) Ratio of the direct and the differential LOD for four different extinction ratios in the intensity-noise-limited regime (red crosses) and $1/\sqrt{4\Delta}$ for comparison (dashed black line).

Figure 4(b) shows the ratio of the direct and the differential LOD for four different extinction ratios in the intensity-noise-limited regime. The improvement towards the direct measurement approaches $1/\sqrt{4\Delta}$ (dashed black line) for decreasing extinction ratio. The

coincidence of the two shot-noise-limited LOD curves in Fig. 4(a) confirms the fundamental limit imposed by linear spectroscopy with classical light.

At our current input power, the optimum LOD is expected to be detector-noise limited, and a factor of 20 better than in the direct measurement. Characterizing the RIN of the destructive interference by calculating the standard deviation of 70 measurements with the OSA, however, yields a value of 8%, which is more than one order of magnitude higher than the 0.21% measured for the RIN in the direct measurement. The additional fluctuations of the destructive interference must be caused by interferometer instabilities which cannot be compensated for by our simple active locking scheme. Consequently, with the current combination of a beam path in air, a one-dimensional PZT lock and a slow OSA for spectral measurements, we are not able to experimentally demonstrate an increased sensitivity in differential spectroscopy. However, in future implementations, the influence of these residual fluctuations on the LOD can be mitigated – or even completely removed – by a mechanically more stable design, by evacuating the interferometer environment, by an improved active stabilization scheme and/or by fast acquisition of spectra such as, e.g., in dual-comb configuration [17,18].

6. Differential molecular fingerprinting

For a proof-of-principle differential molecular fingerprinting measurement, we introduced methane molecules in one arm of the interferometer. To this end, we placed a rudimentary gas cell into one interferometer arm and, for balancing Fresnel reflections and dispersion, two windows equivalent to those of the cell in the other arm. With ambient air in the gas cell the extinction ratio was not notably affected. Filling the 8-cm long gas cell in the sample arm with methane at an estimated pressure of roughly 1 bar resulted in an additional phase difference between the two interferometer arms due to the non-resonant interaction with the methane molecules. The group delay was compensated by geometrically adjusting the OPD.
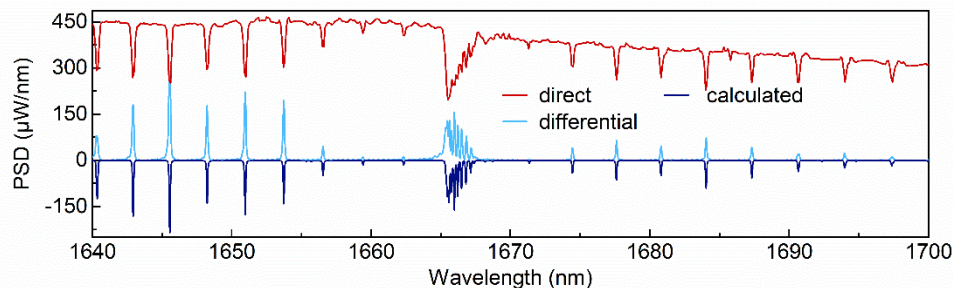

Fig. 5. Methane resonances within the spectral coverage of the utilized OSA, in direct and differential measurement configuration, at ~1 bar. For comparison, the inverted theory curve for the differential measurement is shown.

Figure 5 shows the resonances in the $2\nu_3$ vibrational overtone band of methane within the spectral coverage of the utilized OSA, measured in the interferometric, differential configuration as well as in a direct configuration, i.e. with the reference arm of the interferometer blocked. The theory curve based on Eq. (9) and absorption data from HITRAN [19] shows good qualitative agreement with the measurement. Due to the absence of a suitable pressure gauge and the limited spectral resolution of the OSA, in the following we explain the experimental observations in a qualitative picture rather than quantitatively. Up to a small fraction of energy transferred to molecular vibrations, the instantaneous response of the methane sample is identical to the excitation. Thus, in the differential measurement the instantaneous response destructively interferes with the excitation pulse in the reference arm and the differential signal mainly contains the isolated, resonant response emitted by the vibrationally excited methane molecules [20]. However, in the direct measurement, the

interference of the instantaneous and the phase-shifted, resonant sample response manifests itself as a depletion of the PSD at the resonance frequencies (i.e. absorption in classical spectroscopy).

7. Conclusion and outlook

We showed an unprecedented combination of interferometric deep nulling and broad bandwidth with a Mach-Zehnder-like interferometer. Optimizing the quality of the optics, and utilizing high-precision, kinematic mounts for alignment will push the extinction ratio towards the theoretical limit. Improving the mechanical stability, operating the system in vacuum and enhancing the active path length stabilization scheme will reduce residual fluctuations of the destructive interference. In combination with higher input powers and a better extinction ratio, this promises an improvement of the LOD by at least two orders of magnitude as compared to the direct measurement.

Our proof of principle demonstrates the suitability of the novel concept for a variety of applications. For instance, optical subtraction combined with frequency-comb spectroscopy [21–23] will yield an unprecedented combination of sensitivity and spectral resolution. Furthermore, time-resolved detection of the difference signal [17,18,24–27] promises fully background-free detection of molecular fingerprints, by spatial *and* temporal separation of the latter from an impulsive excitation.

Finally, the techniques presented here might both benefit, and profit from related interferometer work. For instance, the broadband extinction might be useful in Mach-Zehnder-type white-light interferometry, and technical solutions from gravitational wave detectors [28] might help improve the stability of the interferometer.

8. Appendix

8.1 Optimum splitting ratio

We define the optimum power-splitting ratio at the beam splitter (and combiner) as the value that maximizes the power propagating through each arm (with the other arm blocked) to the destructive port. This optimization criterion maximizes the signal related to the light-matter interaction under scrutiny, in the destructive interference arm. In the case of uncoated optics, the power transmission T and reflection R at a material-air interface is defined by the Fresnel equations for the refractive index of the material, the angle of incidence (AOI), and polarization. For our interferometer geometry, the following equation describes the intensities I_1 and I_2 in the interferometer arms 1 and 2 – respectively – reaching the difference port while the other arm is blocked:

$$I_1 = I_0 \left(T\,T\,T\,R\,T\right) = I_2 = I_0 \left(R\,T\,T\,T\,T\right) = I_0 R T^4, \qquad (15)$$

where I_0 is the intensity entering the interferometer. Eq. (15) assumes that the external AOI on all optics are identical, resulting in identical transmission and reflection. Neglecting absorption, $R = 1\text{-}T$ holds and one can easily calculate that I_1 and I_2 are maximized for $R = 0.2$ and $T = 0.8$. For N-BK7 this splitting ratio is achieved at an AOI of 62.5° for s-polarized light.

8.2 Influence of misalignment

To analyze the influence of misalignment of optical elements on the extinction ratio, we built a geometrical optics model of the interferometer using ray transfer matrix analysis. Angular misalignments of the interferometer were included by extending the ABCD-matrices to 3x3-matrices [29]. The observed quantity is the spatial overlap of the two arms after recombination, which is mathematically expressed by the overlap integral over the normalized complex transverse field distributions of both arms [30]. The overlap integral of

two Gaussian beams for a certain angular misalignment normalized to the overlap integral of two perfectly overlapping Gaussian beams (i.e. with equal beam parameters and no misalignment) yields the extinction ratio given by 1 minus the aforementioned normalized overlap integral.

8.3 Influence of beam splitter thickness mismatch

Ideally, the beam splitter and beam combiner should have the exact same thickness and the compensation plate should have exactly twice this thickness. We calculated the influence of deviations from this ideal case on the extinction ratio by comparing the intensities in the destructive and constructive interference arms. The intensity of the destructive interference is that of the difference of the electric fields of the input pulse dispersed by 9 mm borosilicate crown glass (N-BK7) and by 9 mm + Δd N-BK7 where Δd is the thickness tolerance/mismatch. The intensity of the constructive interference is that of the sum of the electric fields of the input pulse dispersed by 9 mm N-BK7 and by 9 mm + Δd N-BK7. The ratio of these two intensities is the extinction ratio plotted in Fig. 2(b).

References

1. H. Bar-Lev, "A dual-beam infrared interferometer-spectrometer," Infrared Phys. **7**(2), 93–98 (1967).
2. H. R. Chandrasekhar, L. Genzel, and J. Kuhl, "Double-beam fourier spectroscopy with interferometric background compensation," Opt. Commun. **17**(1), 106–110 (1976).
3. D. Kuehl and P. R. Griffiths, "Dual-Beam Fourier Transform Infrared Spectrometer," Anal. Chem. **50**(3), 418–422 (1978).
4. V. V. Goncharov and G. E. Hall, "Broadband laser enhanced dual-beam interferometry," Opt. Lett. **37**(12), 2406–2408 (2012).
5. D. L. Beduhn and R. L. White, "Advantages of Dual-Beam Interferometry in Fourier Transform Infrared Spectrometry," Appl. Spectrosc. **40**(5), 628–632 (1986).
6. L. Genzel and J. Kuhl, "A new version of a Michelson interferometer for Fourier transform infrared spectroscopy," Infrared Phys. **18**(2), 113–120 (1978).
7. J. P. Dakin, H. O. Edwards, and B. H. Weigl, "Progress with optical gas sensors using correlation spectroscopy," Sens. Actuators B Chem. **29**(1), 87–93 (1995).
8. Z. Guan, M. Lewander, and S. Svanberg, "Quasi zero-background tunable diode laser absorption spectroscopy employing a balanced Michelson interferometer," Opt. Express **16**(26), 21714–21720 (2008).
9. R. Bracewell, "Detecting nonsolar planets by spinning infrared interferometer," Nature **274**(5673), 780–781 (1978).
10. P. Gabor, *A study of the performance of a nulling interferometer*, Université Paris Sud - Paris XI, Paris, (2009).
11. E. Serabyn and M. M. Colavita, "Fully symmetric nulling beam combiners," Appl. Opt. **40**(10), 1668–1671 (2001).
12. J. Gay and Y. Rabbia, "An interferometric method for coronography", C. R. Acad. Sci. Paris **322**(3), (1996).
13. D. Mawet, C. Hanot, C. Lenaers, P. Riaud, D. Defrère, D. Vandormael, J. Loicq, K. Fleury, J.-Y. Plesseria, J. Surdej, and S. Habraken, "Fresnel rhombs as achromatic phase shifters for infrared nulling interferometry," Opt. Express **15**(20), 12850–12865 (2007).
14. J. Hayden, S. Hugger, F. Fuchs, and B. Lendl, "A quantum cascade laser-based Mach–Zehnder interferometer for chemical sensing employing molecular absorption and dispersion," Appl. Phys. B **124**(2), 29 (2018).
15. T. W. Hänsch and B. Couillaud, "Laser frequency stabilization by polarization spectroscopy of a reflecting reference cavity," Opt. Commun. **35**(3), 441–444 (1980).
16. D. Brida, G. Krauss, A. Sell, and A. Leitenstorfer, "UltrabroadbandEr:fiber lasers," Laser Photonics Rev. **8**(3), 409–428 (2014).
17. A. Muraviev, V. O. Smolski, Z. E. Loparo, and K. L. Vodopyanov, "Massively parallel sensing of trace molecules and their isotopologues with broadband subharmonic mid-infrared frequency combs," Nat. Photonics **12**(4), 209–214 (2018).
18. I. Coddington, W. C. Swann, and N. R. Newbury, "Time-domain spectroscopy of molecular free-induction decay in the infrared," Opt. Lett. **35**(9), 1395–1397 (2010).
19. I. E. Gordon, L. S. Rothman, C. Hill, R. V. Kochanov, Y. Tan, P. F. Bernath, M. Birk, V. Boudon, A. Campargue, K. V. Chance, B. J. Drouin, J.-M. Flaud, R. R. Gamache, J. T. Hodges, D. Jacquemart, V. I. Perevalov, A. Perrin, K. P. Shine, M.-A. H. Smith, J. Tennyson, G. C. Toon, H. Tran, V. G. Tyuterev, A. Barbe, A. G. Császár, V. M. Devi, T. Furtenbacher, J. J. Harrison, J.-M. Hartmann, A. Jolly, T. J. Johnson, T. Karman, I. Kleiner, A. A. Kyuberis, J. Loos, O. M. Lyulin, S. T. Massie, S. N. Mikhailenko, N. Moazzen-Ahmadi, H. S. P. Müller, O. V. Naumenko, A. V. Nikitin, O. L. Polyansky, M. Rey, M. Rotger, S. W. Sharpe, K. Sung, E. Starikova, S. A. Tashkun, J. V. Auwera, G. Wagner, J. Wilzewski, P. Wcisło, S. Yu, and E. J. Zak, "The HITRAN2016 Molecular Spectroscopic Database," J. Quant. Spectrosc. Radiat. Transf. **203**, 3–69 (2017).

20. A. Laubereau and W. Kaiser, "Vibrational dynamics of liquids and solids investigated by picosecond light pulses," Rev. Mod. Phys. **50**(3), 607–665 (1978).

21. T. Udem, R. Holzwarth, and T. W. Hänsch, "Optical frequency metrology," Nature **416**(6877), 233–237 (2002).

22. J. Ye and S. T. Cundiff, "Femtosecond optical frequency comb: principle, operation and applications", Femtosecond Optical Frequency Comb Technology (Springer, 2005).

23. S. A. Diddams, L. Hollberg, and V. Mbele, "Molecular fingerprinting with the resolved modes of a femtosecond laser frequency comb," Nature **445**(7128), 627–630 (2007).

24. M. Tonouchi, "Cutting-edge terahertz technology," Nat. Photonics **1**(2), 97–105 (2007).

25. A. A. Lanin, A. A. Voronin, A. B. Fedotov, and A. M. Zheltikov, "Time-domain spectroscopy in the mid-infrared," Sci. Rep. **4**(1), 6670 (2015).

26. I. Pupeza, M. Huber, W. Schweinberger, M. Trubetskov, S. A. Hussain, L. Vamos, O. Pronin, F. Habel, V. Pervak, N. Karpowicz, M. Zigman, and F. Krausz in 2017 European Conference on Lasers and Electro-Optics – European Quantum Electronics Conference (Optical Society of America, 2017), "Field-Resolved Spectroscopy in the Molecular Fingerprint Region", paper CH-2_4.

27. M. Huber, W. Schweineberger, M. Trubetskov, S. A. Hussein, O. Pronin, E. Fill, A. Apolonski, M. Zigman, and F. Krausz, I. Pupeza in 2017 European Conference on Lasers and Electro-Optics – European Quantum Electronics Conference (Optical Society of America, 2017), "Detection sensitivity of field-resolved spectroscopy in the molecular fingerprint region", paper CH-P_4.

28. B. P. Abbott, R. Abbott, R. Adhikari, P. Ajith, B. Allen, G. Allen, R. S. Amin, S. B. Anderson, W. G. Anderson, M. A. Arain, M. Araya, H. Armandula, P. Armor, Y. Aso, S. Aston, P. Aufmuth, C. Aulbert, S. Babak, P. Baker, S. Ballmer, C. Barker, D. Barker, B. Barr, P. Barriga, L. Barsotti, M. A. Barton, I. Bartos, R. Bassiri, M. Bastarrika, B. Behnke, M. Benacquista, J. Betzwieser, P. T. Beyersdorf, I. A. Bilenko, G. Billingsley, R. Biswas, E. Black, J. K. Blackburn, L. Blackburn, D. Blair, B. Bland, T. P. Bodiya, L. Bogue, R. Bork, V. Boschi, S. Bose, P. R. Brady, V. B. Braginsky, J. E. Brau, D. O. Bridges, M. Brinkmann, A. F. Brooks, D. A. Brown, A. Brummit, G. Brunet, A. Bullington, A. Buonanno, O. Burmeister, R. L. Byer, L. Cadonati, J. B. Camp, J. Cannizzo, K. C. Cannon, J. Cao, L. Cardenas, S. Caride, G. Castaldi, S. Caudill, M. Cavaglià, C. Cepeda, T. Chalermsongsak, E. Chalkley, P. Charlton, S. Chatterji, S. Chelkowski, Y. Chen, N. Christensen, C. T. Y. Chung, D. Clark, J. Clark, J. H. Clayton, T. Cokelaer, C. N. Colacino, R. Conte, D. Cook, T. R. C. Corbitt, N. Cornish, D. Coward, D. C. Coyne, J. D. E. Creighton, T. D. Creighton, A. M. Cruise, R. M. Culter, A. Cumming, L. Cunningham, S. L. Danilishin, K. Danzmann, B. Daudert, G. Davies, E. J. Daw, D. DeBra, J. Degallaix, V. Dergachev, S. Desai, R. DeSalvo, S. Dhurandhar, M. Díaz, A. Dietz, F. Donovan, K. L. Dooley, E. E. Doomes, R. W. P. Drever, J. Dueck, I. Duke, J.-C. Dumas, J. G. Dwyer, C. Echols, M. Edgar, A. Effler, P. Ehrens, E. Espinoza, T. Etzel, M. Evans, T. Evans, S. Fairhurst, Y. Faltas, Y. Fan, D. Fazi, H. Fehrmenn, L. S. Finn, K. Flasch, S. Foley, C. Forrest, N. Fotopoulos, A. Franzen, M. Frede, M. Frei, Z. Frei, A. Freise, R. Frey, T. Fricke, P. Fritschel, V. V. Frolov, M. Fyffe, V. Galdi, J. A. Garofoli, I. Gholami, J. A. Giaime, S. Giampanis, K. D. Giardina, K. Goda, E. Goetz, L. M. Goggin, G. González, M. L. Gorodetsky, S. Goßler, R. Gouaty, A. Grant, S. Gras, C. Gray, M. Gray, R. J. S. Greenhalgh, A. M. Gretarsson, F. Grimaldi, R. Grosso, H. Grote, S. Grunewald, M. Guenther, E. K. Gustafson, R. Gustafson, B. Hage, J. M. Hallam, D. Hammer, G. D. Hammond, C. Hanna, J. Hanson, J. Harms, G. M. Harry, I. W. Harry, E. D. Harstad, K. Haughian, K. Hayama, J. Heefner, I. S. Heng, A. Heptonstall, M. Hewitson, M. Hild, E. Hirose, D. Hoak, K. A. Hodge, K. Holt, D. J. Hosken, J. Hough, D. Hoyland, B. Hughey, S. H. Huttner, D. R. Ingram, T. Isogai, M. Ito, A. Ivanov, B. Johnson, W. W. Johnson, D. I. Jones, G. Jones, R. Jones, L. Ju, P. Kalmus, V. Kalogera, S. Kandhasamy, J. Kanner, D. Kasprzyk, E. Katsavounidis, K. Kawabe, S. Kawamura, F. Kawazoe, W. Kells, D. G. Keppel, A. Khalaidovski, F. Y. Khalili, R. Khan, E. Khazanov, P. King, J. S. Kissel, S. Klimenko, K. Kokeyama, V. Kondrashov, R. Kopparapu, S. Koranda, D. Kozak, B. Krishnan, R. Kumar, P. Kwee, P. K. Lam, M. Landry, B. Lantz, A. Lazzarini, H. Lei, M. Lei, N. Leindecker, I. Leonor, C. Li, H. Lin, P. E. Lindquist, T. B. Littenberg, N. A. Lockerbie, D. Lodhia, M. Longo, M. Lormand, P. Lu, M. Lubinski, A. Lucianetti, H. Lück, B. Machenschalk, M. MacInnis, M. Mageswaran, K. Mailand, I. Mandel, V. Mandic, S. Márka, Z. Márka, A. Markosyan, J. Markowitz, E. Maros, I. W. Martin, R. M. Martin, J. N. Marx, K. Mason, F. Matichard, L. Matone, R. A. Matzner, N. Mavalvala, R. McCarthy, D. E. McClelland, S. C. McGuire, M. McHugh, G. McIntyre, D. J. A. McKechan, K. McKenzie, M. Mehmet, A. Melatos, A. C. Melissinos, D. F. Menéndez, G. Mendell, R. A. Mercer, S. Meshkov, C. Messenger, M. S. Meyer, J. Miller, J. Minelli, Y. Mino, V. P. Mitrofanov, G. Mitselmakher, R. Mittleman, O. Miyakawa, B. Moe, S. D. Mohanty, S. R. P. Mohapatra, G. Moreno, T. Morioka, K. Mors, K. Mossavi, C. MowLowry, G. Mueller, H. Müller-Ebhardt, D. Muhammad, S. Mukherjee, H. Mukhopadhyay, A. Mullavey, J. Munch, P. G. Murray, E. Myers, J. Myers, T. Nash, J. Nelson, G. Newton, A. Nishizawa, K. Numata, J. O'Dell, B. O'Reilly, R. O'Shaughnessy, E. Ochsner, G. H. Ogin, D. J. Ottaway, R. S. Ottens, H. Overmier, B. J. Owen, Y. Pan, C. Pankow, M. A. Papa, V. Parameshwaraiah, P. Patel, M. Pedraza, S. Penn, A. Perraca, V. Pierro, I. M. Pinto, M. Pitkin, H. J. Pletsch, M. V. Plissi, F. Postiglione, M. Principe, R. Prix, L. Prokhorov, O. Punken, V. Quetschke, F. J. Raab, D. S. Rabeling, H. Radkins, P. Raffai, Z. Raics, N. Rainer, M. Rakhmanov, V. Raymond, C. M. Reed, T. Reed, H. Rehbein, S. Reid, D. H. Reitze, R. Riesen, K. Riles, B. Rivera, P. Roberts, N. A. Robertson, C. Robinson, E. L. Robinson, S. Roddy, C. Röver, J. Rollins, J. D. Romano, J. H. Romie, S. Rowan, A. Rüdiger, P. Russell, K. Ryan, S. Sakata, L. S. de la Jordana, V. Sandberg, V. Sannibale, L. Santamaría, S. Saraf, P. Sarin, B. S. Sathyaprakash, S. Sato, M. Satterthwaite, P. R. Saulson, R. Savage, P. Savov, M. Scanlan, R. Schilling, R. Schnabel, R. Schofield, B. Schulz, B. F. Schutz, P. Schwinberg, J. Scott, S. M. Scott, A. C. Searle, B. Sears, F. Seifert, D. Sellers, A. S. Sengupta, A. Sergeev, B. Shapiro, P. Shawhan, D. H. Shoemaker, A. Sibley, X.

Siemens, D. Sigg, S. Sinha, A. M. Sintes, B. J. J. Slagmolen, J. Slutsky, J. R. Smith, M. R. Smith, N. D. Smith, K. Somiya, B. Sorazu, A. Stein, L. C. Stein, S. Steplewski, A. Stochino, R. Stone, K. A. Strain, S. Strigin, A. Stroeer, A. L. Stuver, T. Z. Summerscales, K.-X. Sun, M. Sung, P. J. Sutton, G. P. Szokoly, D. Talukder, L. Tang, D. B. Tanner, S. P. Tarabrin, J. R. Taylor, R. Taylor, J. Thacker, K. A. Thorne, A. Thüring, K. V. Tokmakov, C. Torres, C. Torrie, G. Traylor, M. Trias, D. Ugolini, J. Ulmen, K. Urbanek, H. Vahlbruch, M. Vallisneri, C. V. D. Broeck, M. V. van der Sluys, A. A. van Veggel, S. Vass, R. Vaulin, A. Vecchio, J. Veitch, P. Veitch, C. Veltkamp, A. Villar, C. Vorvick, S. P. Vyachanin, S. J. Waldman, L. Wallace, R. L. Ward, A. Weidner, M. Weinert, A. J. Weinstein, R. Weiss, L. Wen, S. Wen, K. Wette, J. T. Whelan, S. E. Whitcomb, B. F. Whiting, C. Wilkinson, P. A. Willems, H. R. Williams, L. Williams, B. Willke, I. Wilmut, L. Winkelmann, W. Winkler, C. C. Wipf, A. G. Wiseman, G. Woan, R. Wooley, J. Worden, W. Wu, I. Yakushin, H. Yamamoto, Z. Yan, S. Yoshida, M. Zanolin, J. Zhang, L. Zhang, C. Zhao, N. Zotov, M. E. Zucker, H. Mühlen, and J. Zweizig, "LIGO: the Laser Interferometer Gravitational-Wave Observatory," Rep. Prog. Phys. **72**(7), 76901 (2009).
29. H. Kogelnik and T. Li, "Laser beams and resonators," Appl. Opt. **5**(10), 1550–1567 (1966).
30. W. B. Joyce and B. C. DeLoach, "Alignment of Gaussian beams," Appl. Opt. **23**(23), 4187–4196 (1984).